PCCP

PAPER

View Article Online
View Journal | View Issue

Cite this: *Phys. Chem. Chem. Phys.*, 2019, **21**, 21355

Vibronic spectroscopy of methyl anthranilate and its water complex: hydrogen atom dislocation in the excited state†

Karl N. Blodgett,[a] Dewei Sun,[a] Joshua L. Fischer,[a] Edwin L. Sibert III[b] and Timothy S. Zwier *[a]

Laser-induced fluorescence (LIF) excitation, dispersed fluorescence (DFL), UV–UV-hole burning, and UV-depletion spectra have been collected on methyl anthranilate (MA, methyl 2-aminobenzoate) and its water-containing complex (MA–H_2O), under jet-cooled conditions in the gas phase. As a close structural analog of a sunscreen agent, MA has a strong absorption due to the S_0–S_1 transition that begins in the UV-A region, with the electronic origin at 28 852 cm^{-1} (346.6 nm). Unlike most sunscreens that have fast non-radiative pathways back to the ground state, MA fluoresces efficiently, with an excited state lifetime of 27 ns. Relative to methyl benzoate, inter-system crossing to the triplet manifold is shut off in MA by the strong intramolecular NH···O=C H-bond, which shifts the $^3n\pi^*$ state well above the $^1\pi\pi^*$ S_1 state. Single vibronic level DFL spectra are used to obtain a near-complete assignment of the vibronic structure in the excited state. Much of the vibrational structure in the excitation spectrum is Franck–Condon activity due to three in-plane vibrations that modulate the distance between the NH_2 and CO_2Me groups, ν_{33} (421 cm^{-1}), ν_{34} (366 cm^{-1}), and ν_{36} (179 cm^{-1}). Based on the close correspondence between experiment and theory at the TD-DFT B3LYP-D3BJ/def2TZVP level of theory, the major structural changes associated with electronic excitation are evaluated, leading to the conclusion that the major motion is a reorientation and constriction of the 6-membered H-bonded ring closed by the intramolecular NH···O=C H-bond. This leads to a shortening of the NH···O=C H-bond distance from 1.926 Å to 1.723 Å, equivalent to about a 25% reduction in the H···O distance compared to full H-atom transfer. As a result, the excited state process near the S_1 origin is a hydrogen atom dislocation that is brought about primarily by heavy atom motion, since the shortened H-bond distance results from extensive heavy-atom motion, with only a 0.03 Å increase in the NH bond length relative to its ground state value.

Received 16th August 2019,
Accepted 11th September 2019

DOI: 10.1039/c9cp04556b

rsc.li/pccp

I. Introduction

Methyl anthranilate (MA) is the precursor to menthyl anthranilate (MenA), an FDA approved sunscreen agent.[1] Upon UV absorption, efficient sunscreen molecules are able to non-radiatively decay back to their ground electronic state, thereby regenerating their UV-absorbing capacities. In some cases, internal conversion is thought to be facilitated on the S_1 surface by H-atom transfer.[2–8] As such, much theoretical and experimental work has been directed toward understanding excited state hydrogen atom, or proton, transfer processes in this family of molecules. There are circumstances, however, in which excited state intramolecular H-atom transfer does not completely quench fluorescence, but instead leads to a Stokes-shifted fluorescence that signals its occurrence, as in the case of salicylic acid and methyl salicylate.[3,4,9,10] This shifted emission provides a ready means of assessing the efficiency of the process as a function of vibrational level in the excited state.

For a hydrogen atom transfer process to occur, a donor hydrogen must be oriented toward an acceptor atom. Upon electronic excitation the donor X–H becomes more acidic while the acceptor Y becomes more basic, and the X–H bond is broken, resulting in the transfer of the hydrogen to the acceptor atom.[11,12] In so doing, the excited state geometry rearranges as it moves on the potential energy surface, producing broad, red-shifted emission back to highly excited vibrational states in the ground state. This red-shifted emission is characteristic of these transient hydrogen transfer products. Alternatively, the excited state molecule may, through displacements along one or more internal coordinates, reach a conical intersection and non-radiatively decay back to the electronic ground state.[3,11–13]

[a] *Department of Chemistry, Purdue University, West Lafayette, Indiana 47907-2084, USA. E-mail: zwier@purdue.edu*
[b] *Department of Chemistry, University of Wisconsin-Madison, Madison, Wisconsin 53706, USA*

† Electronic supplementary information (ESI) available. See DOI: 10.1039/c9cp04556b

There is a body of evidence, however, that suggests that in some cases, rather than a complete hydrogen atom transfer, it is a hydrogen atom dislocation that occurs upon electronic excitation, where the X–H bond distance is increased, but not to the point of breaking and forming new covalent bonds.[14–19] In many ways, this is a fascinating circumstance in which the structural change on the excited state surface heads toward chemical reaction, but in not achieving it, enables detailed structural characterization. By dispersing the emission from the excited state vibrational levels, one observes the projection of each level back into the ground state in regions where the ground state vibrations still can be used as a set of modes to characterize the excited state structural change. In a previous study of the infrared (IR) and electronic spectroscopy of anthranilic acid and its water complex in the ground (S_0) and first excited (S_1) electronic states, the body of spectroscopic evidence pointed to a hydrogen atom dislocation, rather than transfer, occurring upon electronic excitation.[14,15] However, no dispersed fluorescence scans were carried out, limiting the degree to which structural characterization was possible.

In the present study, we carry out just such a study on a close analog of anthranilic acid, methyl anthranilate, which replaces the carboxylic acid hydrogen with a methyl group. MA, shown in Fig. 1, has a 6-membered hydrogen bonded ring closed by an NH···O=C H-bond. In this first of two papers on MA, we report a detailed study of the vibrationally-resolved electronic spectroscopy of MA and its single-water complex, MA–H_2O, in both the ground and excited electronic states. Using a suite of laser-based techniques, coupled with density functional theory calculations, we interrogate the vibronic structure of jet-cooled MA and MA–H_2O, and extract and discuss the structural implications of the spectra.

II. Experimental and computational methods

Methyl anthranilate was purchased from Sigma-Aldrich (≥99% purity) and used without further purification. The instrument used to collect fluorescence data has been described in detail elsewhere.[20] The sample was entrained in 2.0 bar backing pressure of helium and expanded through an 800 μm orifice of a pulsed valve (Parker series 9 General valve) into a vacuum chamber pumped by a roots blower. In the ensuing supersonic expansion, collisions with the helium backing gas serve to cool MA to its ground state zero-point vibrational energy level. The MA–H_2O complex was observed in the expansion without changing experimental conditions, formed by residual H_2O present in the lines and sample. The identity of the MA monomer and water complex were verified by mass-resolved excitation spectra (see ESI,† Section S1). The collisionally cooled molecules are interrogated by one or more lasers propagating perpendicular to the expansion, intersecting the expansion approximately 8 mm downstream from the source. Emission is collected at the focal point of two 4-inch diameter spherical mirrors, the bottom of which has a 1 cm hole through which resonant fluorescence is steered. This light is collimated through a plano-convex lens, passed through long-pass filters to reduce scattered laser light, and imaged onto a photomultiplier tube. Laser induced fluorescence (LIF) excitation spectra were collected by scanning the output of a 20 Hz frequency doubled Nd:YAG-pumped dye laser (Radiant Dyes NarrowScan) across the 28 500–30 000 cm^{-1} region associated with the S_0–S_1 transition of MA, where total collected fluorescence is plotted as a function of excitation wavelength.

Since the LIF spectrum contains contributions from all possible conformational isomers (conformers) and complexes of MA, double resonance laser techniques were employed to decompose the spectrum into its component parts. UV–UV hole-burning (UV–UV HB), IR-UV holeburning (IR-UV HB), and UV depletion (UV-D) spectroscopies were used for this purpose. In UV–UV HB, a 10 Hz hole-burn laser (Lambda Physik Scanmate) has its wavelength fixed on some vibronic transition in the LIF spectrum. This hole-burn laser temporally precedes by 100 ns, a 20 Hz probe laser which is scanned through the region of interest. When the probe laser wavelength is resonant with a vibronic transition which shares the same ground state as the transition on which the hole-burn laser is fixed, a decrease in fluorescence results from the depletion of ground state zero-point populated molecules. This difference is measured by passing the 20 Hz fluorescence signal through a gated integrator operating in active baseline subtraction mode, the output of which is equivalent to a conformer- or complex-specific UV excitation spectrum. IR-UV HB is the same as UV–UV HB, except that the 10 Hz hole-burn laser is now an IR laser (LaserVision OPO) which has its frequency fixed on a unique vibrational transition of the species of interest.

UV-D is similar to UV–UV HB, except that the 10 Hz hole-burn laser is scanned through the region of interest, while the 20 Hz probe laser is fixed on some vibronic transition, whose constant fluorescence signal is monitored. As in UV–UV HB, a conformer-specific UV spectrum is generated. The UV-D spectrum has the advantage that it enables acquisition of the true absorption spectrum, regardless of whether the tuned HB laser accesses states that fluoresce appreciably or not. In this experimental scheme, the signal is a ground state depletion, which is governed solely by the absorption properties of the molecule, rather than the modulation of excited state-dependent fluorescence. Comparison of the UV-D to the UV–UV HB spectrum gives insight into the nature and extent of non-radiative processes that may occur in the excited state.

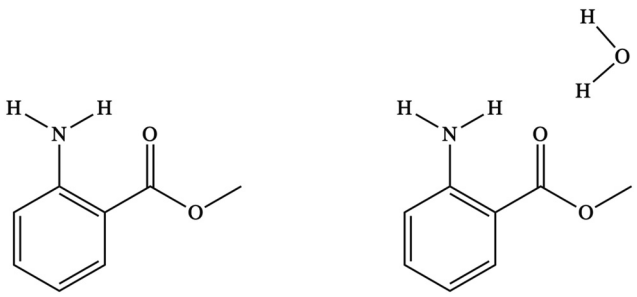

Fig. 1 Chemical structures of methyl anthranilate (MA) and methyl anthranilate–water complex (MA–H_2O).

A disadvantage of the method is that the UV-D spectrum measures depletion of a constant non-zero signal, and therefore has the inherent noise associated with subtraction of two large signals.

Dispersed fluorescence (DFL) spectra were used to aid in the assignment of the transitions in the excitation spectrum by resolving the emission from individual excited state levels prepared by the laser. In this scheme, an excitation laser has its wavelength fixed on some vibronic transition of interest. The emitted fluorescence is dispersed by passing it through a 3/4-meter monochromator outfitted with a grating blazed for UV detection. The dispersed emission is then imaged at the output focal plane onto a gated-intensified CCD camera. This technique determines the ground state vibrational levels formed by emission from a single, laser-prepared excited state vibrational level.

Conformational searches of MA and MA–H_2O were performed using a torsional-sampling Monte Carlo Multiple Minimum algorithm with the OPLS3 force field within the MacroModel computational suite. These calculated structures served as the starting structures for geometry optimization *via* density functional theory (DFT) calculations, using the Becke 3LYP (B3LYP) hybrid functional supplemented with the D3 version of Grimme's dispersion correction[21] and Becke–Johnson (BJ) damping.[22] This functional was used in conjunction with the def2TZVP basis set to calculate harmonic vibrational frequencies of the optimized ground state structures. Time dependent DFT (TD-DFT) calculations were then used to calculate vertical and adiabatic excitation energies as well as the geometry and harmonic vibrational frequencies of the first excited singlet state of multiple MA and MA–H_2O conformers. The Gaussian16 suite of programs was used for the DFT calculations and the visualization of normal modes.[23] Molecular orbitals and optimized structures were visualized using the Gaussian16 suite and Chemcraft Software.[24]

III. Results and analysis

A. Methyl anthranilate monomer

1. Computational predictions. In its ground state, MA may exist as either of two rotamers: one where the amine group hydrogen bonds with the ester oxygen, and the other in which the amine group hydrogen bonds with the carbonyl oxygen (see Fig. S2, ESI†). At the DFT B3LYP-D3BJ/def2TZVP level of theory, the second rotamer is calculated to be 13.3 kJ mol^{-1} lower in energy than the first rotamer. In the supersonic free jet environment, one would anticipate all of the population funneling to the lower energy rotamer. Key structural parameters predicted by the calculations for the C═O bound rotamer in the ground (S_0) and first excited (S_1) singlet states are shown in Fig. 2. The S_1 geometry is predicted to be planar, while the S_0 equilibrium geometry deviates slightly from planarity along the NH_2 inversion coordinate. Relaxed potential energy scans performed along the CNHH improper dihedral angle reveal a wide symmetric double minimum potential in the S_0 electronic state with minima at ±18° and a tiny 5 cm^{-1} inversion barrier centered at the planar geometry (see Fig. S3, ESI†). Since this barrier is well below the zero-point energy, we should anticipate a quasi-planar S_0 geometry with a vibrationally averaged planar configuration, with no inversion tunneling splitting.

Since both the S_0 and S_1 geometries have one mirror plane, they both belong to the C_s point group. As such, the 54 normal modes reduce to 36 totally symmetric (a′, in-plane) and 18 non-totally symmetric (a″, out-of-plane) vibrations. Symmetry also

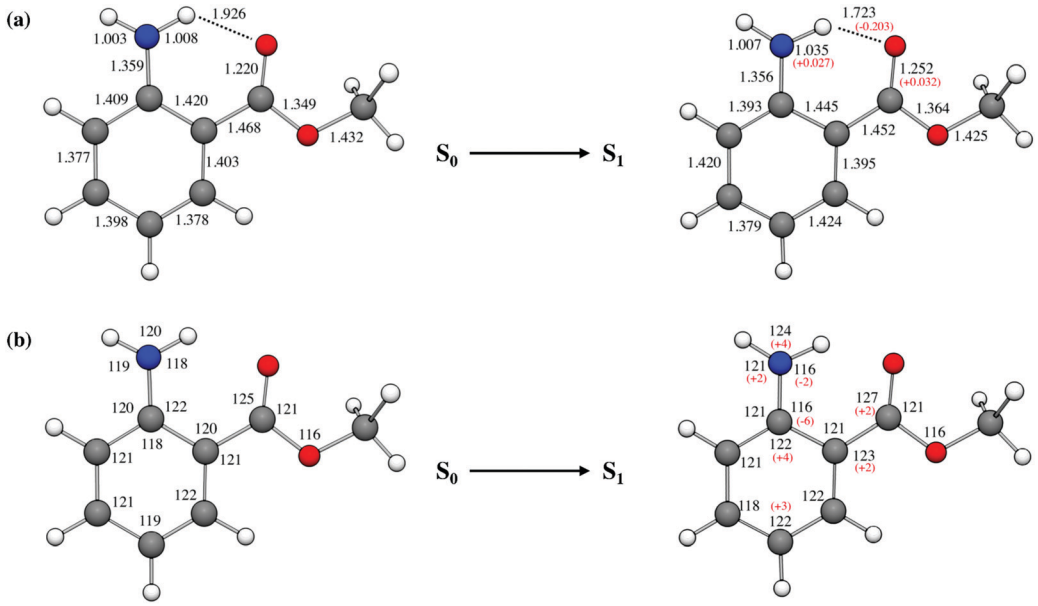

Fig. 2 Optimized ground and S_1 excited state geometries of MA with (a) bond distances and (b) bond angles labelled. Bond lengths are in angstroms (Å) and angles are in degrees. The difference between select ground and excited state parameters are shown in red parentheses. Values were calculated at the DFT B3LYP-D3BJ/def2TZVP level of theory.

constrains the vibronic transitions. According to electric dipole selection rules within the Franck–Condon approximation, allowed transitions originating from the zero-point level include the fundamentals of all in-plane vibrations and only even combinations of out-of-plane vibrations *via* overtones or combination bands. It is worth noting that intensity in combination bands depends on Duschinsky mode mixing for their intensity.[25] In this manuscript, we use Mulliken notation[26] to describe and order the normal modes of vibration.

Vertical TD-DFT B3LYP-D3BJ/def2TZVP calculations predict that the S_1 electronic state is optically accessible from S_0 *via* a $\pi\pi^*$ electron transition with contributions from HOMO → LUMO and (HOMO−1) → (LUMO+1) transitions. This S_0–S_1 transition has an appreciable oscillator strength (f_{01} = 0.1036). Furthermore, the S_1 state is well isolated from other excited states, with S_2 and S_3 1.15 and 1.30 eV above S_1 (see Section S4 for molecular orbital transitions in MA, ESI†). Due to the large energy separation between S_1 and S_2/S_3, and smaller oscillator strengths from S_0, one would not anticipate significant manifestations of vibronic coupling in the S_0–S_1 vibronic spectrum.

2. UV excitation spectroscopy. The LIF excitation spectrum of MA is presented in Fig. 3a. The spectrum spans from 28 825–30 000 cm^{-1} (346.9–333.0 nm), with the S_0–S_1 electronic origin transition appearing at 28 852 cm^{-1}. The lifetime of the S_1 state is measured to be 27 ns (see Fig. S8a for the fluorescence decay trace, ESI†). Fig. 3b shows the UV–UV HB spectra of MA, recorded with the HB laser fixed on the transition at 28 852 cm^{-1}. This spectrum shows that the majority of the peaks in the LIF excitation spectrum are due to the MA monomer. This assignment was verified *via* mass-resolved two-color resonant two-photon ionization (2C-R2PI) excitation spectra (see Fig. S1a, ESI†). The minor peaks in the LIF spectrum that do not burn out in the UV–UV HB scan belong to the MA–H_2O complex (discussed in detail in Section B). To distinguish whether the decrease in intensity in the spectra with increasing excitation energy is due to the drop-off in Franck–Condon factors or some non-radiative decay process, we collected UV-D spectra, shown in Fig. 3c. The UV-D spectrum contains the same peaks and intensity pattern as the UV–UV HB spectra. This indicates that, in the wavelength region we have probed, there is no turn-on of a non-radiative process at play, and that the intensities in the LIF and UV–UV HB spectra presented in Fig. 3a and b are determined primarily by the absorption properties of MA.

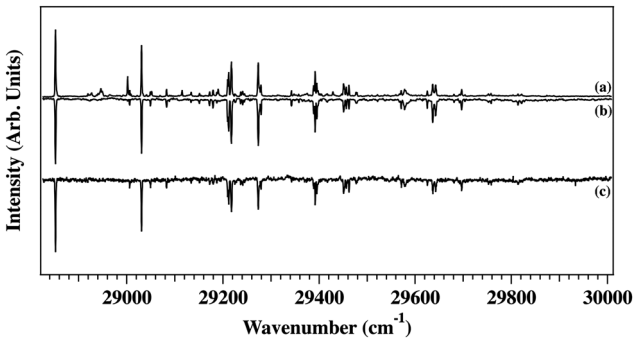

Fig. 3 (a) LIF excitation, (b) UV–UV hole-burning, and (c) UV depletion spectra of MA from 28 825–30 000 cm^{-1}.

The assigned IR-UV HB spectrum of MA is displayed in Fig. 4. These assignments were reached based on corroborating evidence from S_0 and S_1 vibrational frequency calculations, excitation spectra, and DFL spectra, as will be discussed in detail below. A rotational band contour (RBC) scan of the electronic origin transition, taken at a laser resolution of 0.15 cm^{-1} (in the UV) is shown as the top trace in Fig. S9 (ESI†). Using the spectral fitting program JB95,[27] along with transition dipole moment ($a:b:c$ = 77 : 23 : 0) components and rotational constants from the calculated ground and excited states, we obtained the simulated RBC shown as the bottom trace in Fig. S9 (ESI†). The excellent match between experiment and theory bolsters the assignment of MA to the lower energy rotamer.

Table 1 lists the experimental and calculated S_0 and S_1 vibrational frequencies. The excitation spectrum of MA is composed of progressions in in-plane vibrations, even combination bands and overtone transitions of out-of-plane vibrations, and (1 + 1):1

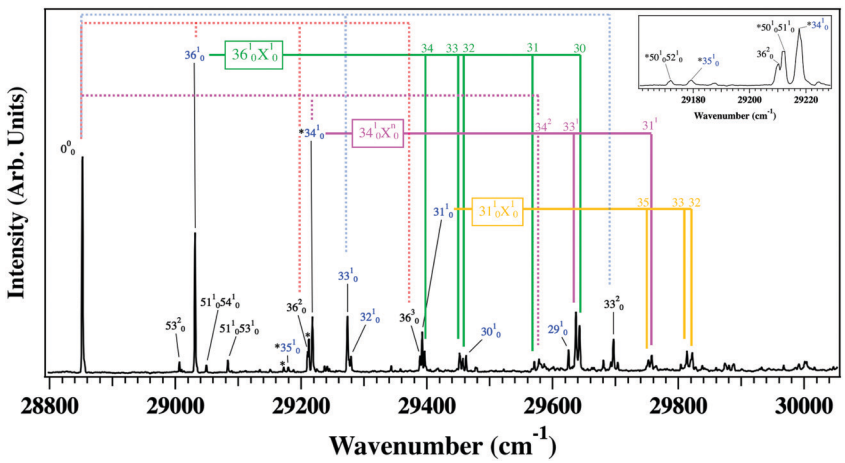

Fig. 4 Assigned S_0–S_1 LIF excitation spectrum of MA. Progressions in the in-plane modes ν_{36} (179 cm^{-1}), ν_{34} (366 cm^{-1}), and ν_{33} (421 cm^{-1}) are displayed *via* red, pink, and blue dotted tie-lines, respectively, while in-plane combination bands built off 36^1_0, 34^1_0, and 31^1_0 are shown with solid tie lines. The identity of mode X is listed above each respective tie line. The inset provides a close-up view of the two pairs of peaks identified as Fermi-resonance pairs.

Table 1 Experimental and calculated S_0 and S_1 frequencies of MA, best fit normal coordinate displacement values, and excited to ground state normal mode projections

S_0			S_1			
a′ in-plane modes						
Mode	Exp. freq. (cm^{-1})	Calc. freq.[a] (cm^{-1})	Exp. freq. (cm^{-1})	Calc. freq.[a] (cm^{-1})	Best-fit displacement[b]	$S_1 \rightarrow S_0$ mode projections[c]
36	179	183	179	183	0.97	33,31,29
35	333	340	327	333	0.10	
34	361	359	366	364	0.85	36, 33, 31, 29
33	412	420	421	423	1.27	36, 34, 31, 29
32	494	506	427	502	0.50	36, 33, 31
31	567	574	540	559	0.60	33, 30
30	672	684	610	641	0.10	29
29	808	818	773	786	0.50	33
18	1355	1353	—	1381	—	—
a″ out of plane modes						
Mode	Exp. freq. (cm^{-1})	Calc. freq. (cm^{-1})	Exp. freq. (cm^{-1})	Calc. freq. (cm^{-1})	Best-fit D	$S_1 \rightarrow S_0$ mode projections
54	57	65	44	49	0	51, 52, 53
53	96	97	77	82	0	51, 53, 54
52	143	145	114	117	0	50, 51
51	161	163	153	156	0	50, 52, 53, 54
50	229	254	207	220	0	51, 52

[a] Frequencies calculated at the DFT B3LYP-D3BJ/def2TZVP level of theory. [b] Value calculated using the Franck–Condon fitting procedure discussed in Section S15 (ESI). [c] Determined from DFL data.

Fermi resonance pairs between out-of-plane combination bands and in-plane fundamentals. Progressions in the in-plane modes ν_{36} (179 cm^{-1}), ν_{34} (366 cm^{-1}), and ν_{33} (421 cm^{-1}) are displayed *via* red, pink, and blue dotted tie-lines, respectively, while in-plane combination bands built off 36_0^1, 34_0^1, and 31_0^1 are shown with solid tie lines. All other assigned peaks, belonging either to in-plane fundamentals or out-of-plane combination bands, are labelled with tags.

It is noteworthy that, while the 0_0^0 transition is the largest peak in the spectrum, all eight of the lowest frequency in-plane fundamentals (ν_{36-29}) have measurable intensity in their X_0^1 fundamentals, indicating a geometry change along these normal coordinates between the ground and excited electronic states. The two pairs of peaks designated with asterisks (and shown in the figure inset) are identified as Fermi-resonance pairs. The five lowest frequency out-of-plane modes, ν_{54-50}, appear as combination and, in the case of ν_{53}, overtone bands.

3. DFL of the 0_0^0 band and in-plane fundamentals. The assigned DFL spectrum of the electronic origin transition is shown in Fig. 5. The peak positions and intensity pattern displayed in the first 1200 cm^{-1} of the DFL spectrum largely mirror those of the excitation spectrum, as would be the case if Franck–Condon factors between the ground and excited state play a dominant role in the observed vibronic structure. This DFL spectrum shows progressions in three in-plane modes; ν_{36}, ν_{34}, ν_{33}, all of which also showed clear progressions in the

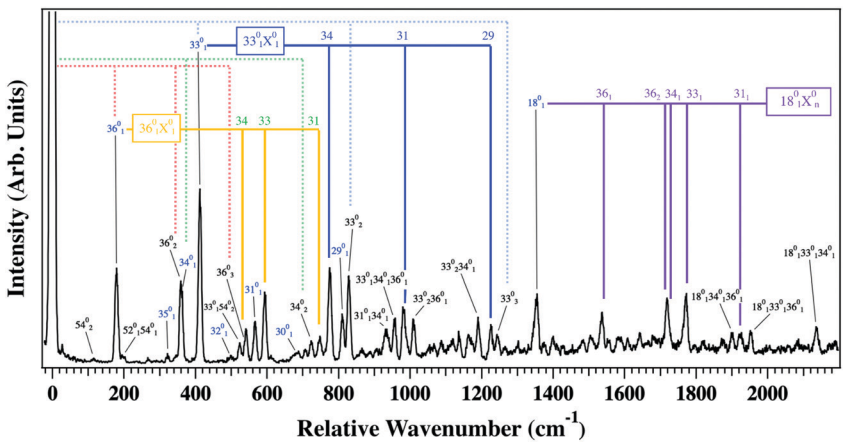

Fig. 5 Dispersed fluorescence spectrum of the S_0–S_1 origin transition of MA. Progressions in the in-plane modes ν_{36} (179 cm^{-1}), ν_{34} (361 cm^{-1}), and ν_{33} (412 cm^{-1}) are displayed *via* red, green, and blue dotted tie-lines, respectively, while in-plane combination bands built off 36_0^1, 33_0^1, and 18_0^1 are shown with solid tie lines. The identity of mode X is listed above each respective tie line.

excitation spectrum. Additionally, each in-plane fundamental that we observe in the excitation spectrum appears with an analogous $\Delta\nu = 1$ transition in the origin DFL spectrum, with one additional higher frequency band appearing at +1355 cm^{-1} (ν_{18}). As was the case with the excitation spectrum, we also observe in-plane and out-of-plane combination bands and out-of-plane overtones in the DFL spectrum. The DFL spectrum also has a large number of in-plane combination bands, with a smaller number of out-of-plane combination bands.

Fig. 6 presents the DFL spectra of the eight Franck–Condon active in-plane fundamentals present in the excitation spectrum. In the +327 cm^{-1} DFL spectrum (Fig. 6b) there is a large peak at 333 cm^{-1} with no further progressions at that frequency. The majority of the remainder of the peaks built off of this transition, labelled with red dotted tie lines, are identical in relative frequency and intensity pattern to the entire set of peaks in the 0_0^0 DFL spectrum, indicating that the 333 cm^{-1} peak serves as a false origin (labelled with a red 0_0^0 in Fig. 6). The strong intensity of the peak at 333 cm^{-1}, combined with the excellent agreement between calculated and experimental frequency, leads us to assign the +327 cm^{-1} transition to the 35_0^1 in-plane fundamental, and the 333 cm^{-1} peak as a $\Delta\nu = 0$ transition (35_1^1). The intensity pattern this mode displays in the vibronic spectra, together with the 35_1^1 transition serving as a false origin, indicate a very small displacement of its respective potential wells between S_0 and S_1 states. The $\Delta\nu = 0$ transition of several other excited state modes, ν_{31}, ν_{30}, ν_{29} (Fig. 6f–h), also serve as false origins involving each of these vibrations.

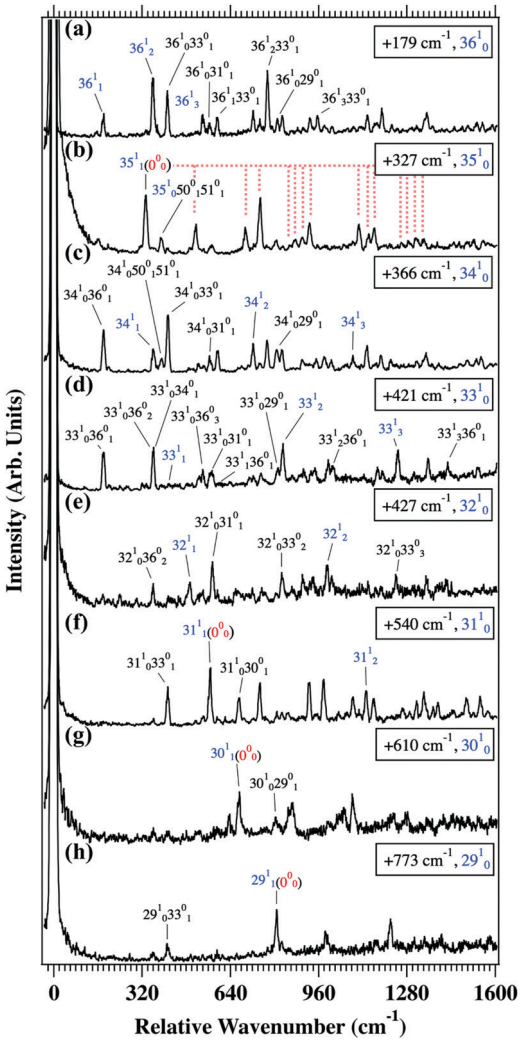

Fig. 6 DFL spectra of the Franck–Condon active, in-plane fundamentals in MA: (a) 36_0^1, (b) 35_0^1, (c) 34_0^1, (d) 33_0^1, (e) 32_0^1, (f) 31_0^1, (g) 30_0^1, and (h) 29_0^1. Ground state progressions in analogous modes are labelled in blue text, and transitions which serve as false origins are marked with a red (0_0^0).

Many of these DFL spectra contain, among other transitions, progressions in their analogous ground state normal mode (labelled in blue in Fig. 6). The DFL spectrum of the transition at +179 cm^{-1}, for example, displays a Franck–Condon progression in a 179 cm^{-1} mode in S_0. Based on the extent of the Franck–Condon activity in the excitation and 0_0^0 DFL spectra in 179 cm^{-1}, one should expect concomitant progressions in the ground state when projecting from $\nu = 1$ in S_1. This evidence, in addition to the agreement between calculated and experimental frequencies, leads us to assign the +179 cm^{-1} transition in the excitation spectrum to the 36_0^1 in-plane fundamental. The long progressions in the vibronic spectra of ν_{36} (with 36_n^1 members up through $n = 3$) implies an appreciable displacement of the respective normal mode coordinates upon electronic excitation.

This one-dimensional normal coordinate displacement, however, does not account for all of the peaks in the 36_0^1 DFL spectrum. There are also several cross-sequence bands present, most notably $36_n^1 33_1^0$, $36_0^1 31_1^0$ and $36_0^1 29_1^0$. Such cross-sequence bands are signatures of Duschinsky mixing, in which the normal coordinates in the S_1 state are linear combinations of the ground state normal coordinates.[28] This may be thought of as a rotation of the normal coordinates on the S_1 potential energy surface (PES) relative to the S_0 PES, where the one-to-one correspondence between ground and excited state normal modes is lost to some degree.[29] The situation is further complicated for in-plane modes, where, in addition to mixing, displacements along the normal coordinate(s) may occur. We may deduce, then, *via* its Franck–Condon activity and cross-sequence bands, that the ν_{36} coordinate in S_1 is both rotated and its origin displaced relative to its corresponding coordinate in S_0.

The prevalence of cross-sequence bands in the in-plane fundamental DFL spectra presented in Fig. 6 implies a significant degree of Duschinsky mixing upon electronic excitation. Using similar logic as that outlined above, we have assigned nearly all of the transitions in the excitation and DFL spectra. Confidence in these assignments is bolstered by the close agreement between calculated and experimentally assigned vibrational frequencies (Table 1). Fig. 7 shows the ground state form of the Franck–Condon active in-plane normal modes. Based on the Franck–Condon activity, the largest displacements are in modes 36 (179 cm^{-1}) and 33 (421 cm^{-1}), similar to what is observed in anthranilic acid.[15]

Through the DFL spectra, we were also able to identify the onset of intramolecular vibrational energy redistribution (IVR) in the S_1 state. IVR results when the laser-prepared state carrying the oscillator strength in excitation anharmonically

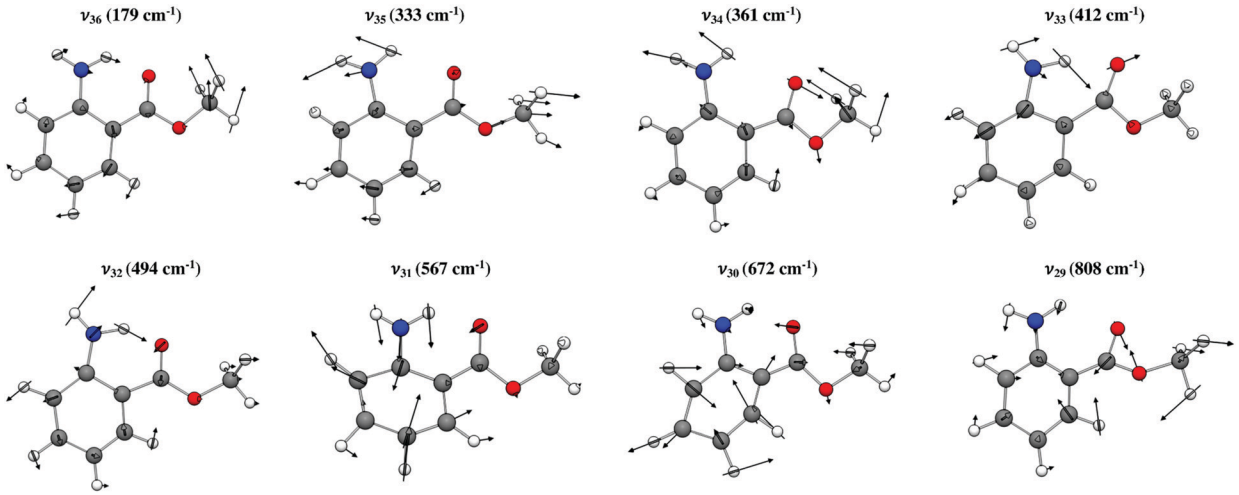

Fig. 7 Ground state in-plane normal modes ν_{36}–ν_{29} of MA. Normal modes were calculated at the DFT B3LYP-D3BJ/def2TZVP level of theory.

couples with a bath of background states at that energy. This bright state/background state mixing of the upper state wave function has the effect of taking what would be sharp vibronic transitions and broadening/shifting transitions due to the state's background character. Fig. S10 (ESI†) presents a sequence of DFL spectra taken at increasing energies relative to the origin. At pump energies greater than 600 cm^{-1} we note the appearance of a broad, increasing baseline, most likely associated with the onset of IVR. The spectral signature of IVR is less clear in the context of MA than it is in many phenyl derivatives,[30,31] due to the much larger geometry change between S_0 and S_1 in MA.

4. DFL of the out-of-plane combination bands and Fermi resonance pairs. The assigned DFL spectra of the transitions assigned to out-of-plane modes are shown in Fig. 8. It is noteworthy that all assigned transitions involve even overtone and combination bands in the out-of-plane modes, providing convincing experimental evidence that the molecule retains C_s symmetry in both ground and excited states. Whereas in-plane modes may undergo both mixing and displacement upon electronic excitation in systems where C_s symmetry is preserved in both states, out-of-plane modes have zero displacement of normal coordinates upon excitation. This zero displacement results in transitions involving out-of-plane modes having weak intensity in the excitation or 0^0 DFL spectra.

In all of the DFL spectra in Fig. 8 there are strong bands in the low frequency region that serve as false origins for transitions built off of them; that is, one can readily assign Franck–Condon activity built off these transitions that mirror the Franck–Condon activity present in the 0^0 DFL spectrum (Fig. 5). It is noteworthy that, in all the spectra in Fig. 8, the most intense false origin is not the $\Delta\nu = 0$ transition (*e.g.*, $X_1^1Y_1^1$ following excitation of $X_0^1Y_0^1$) but instead, one or more cross-sequence band(s).

The abundant cross-sequence transitions assigned in Fig. 8 indicate extensive Duschinsky mixing among the out-of-plane modes. Fig. 9 shows the form of these normal modes in the ground state, along with the reduced Duschinsky rotation matrix calculated at the B3LYP-D3BJ/def2TZVP level of theory. The matrix elements across a row (non-negligible off-diagonal components highlighted in blue) give the expansion coefficients of the indicated S_1 normal coordinate in terms of the S_0 coordinates. Without direct data on cross-sequence hot bands of the type $X_0^1Y_1^0$, it is difficult to carry out quantitative tests of the Duschinsky mixing.[29,32] Nevertheless, we can use this matrix to see whether it is qualitatively consistent with the experimental data; that is, by looking at which modes show clear evidence of mixing with one another. For example, the largest peak in the 53_0^2 DFL spectrum is the cross-sequence band $53_0^254_2^0$, consistent with the large off-diagonal mixing (−0.230) between these two modes. Indeed, DFL spectra from levels with excitation in modes 52, 53, and 54 show significant mixing between all three, as the Duschinsky matrix predicts.

The spectra in Fig. 8d and e show strong false origins in bands that cannot be understood purely in terms of Duschinsky mixing. Indeed, as the inset in Fig. 4 shows, in the excitation spectrum, the $50_0^152_0^1$ and $50_0^151_0^1$ transitions appear in close proximity with the in-plane fundamentals 35_0^1 and 34_0^1, respectively, marked with asterisks. The first set of peaks are assigned to the 50_0^1 52_0^1 combination and Franck–Condon allowed 35_0^1 fundamental transitions. The DFL spectra coming out of this pair (shown in Fig. 10a and b) provide evidence that they are in Fermi-resonance with one another. These spectra share almost all of the same transitions to the ground state, thus revealing their mixed character in the excited state. To substantiate this claim, consider the $50_0^152_0^135_1^0$ transition in the $50_0^152_0^1$ DFL spectrum. The excitation spectrum (Fig. 4), origin and 35_0^1 DFL spectra (Fig. 5 and 6b) all show that ν_{35} has essentially no oscillator strength in its $\Delta\nu = 1$ transitions. The substantial intensity of this transition in the $50_0^152_0^1$ DFL spectrum, then, implies that the upper state contains some 35^1 character. Furthermore, the lack of a $\Delta\nu = 0$ $50_1^152_1^1$ transition in either DFL spectrum, but the corresponding presence of a $50_1^151_1^1$ transition in both, implies strong Duschinsky mixing between modes 51 and 52, as predicted by the Duschinsky matrix in Fig. 9.

The second set of peaks is assigned to an excited state Fermi resonance between the 50^151^1 combination level and the 34^1 in-plane fundamental. The DFL spectra coming out of these levels

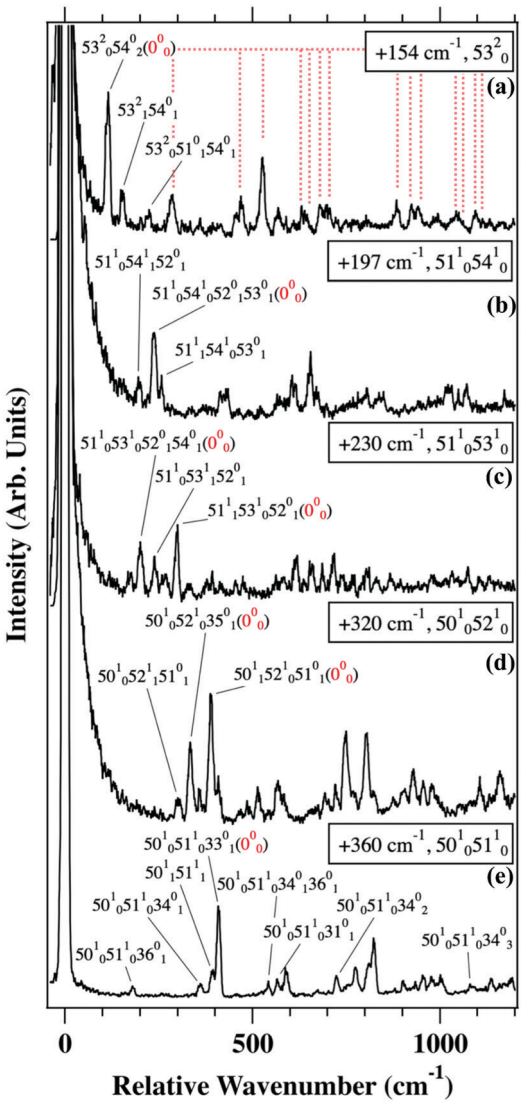

Fig. 8 DFL spectra of transitions involving out-of-plane modes in MA: (a) 53^2_0, (b) $51^1_0 54^1_0$, (c) $51^1_0 53^1_0$, (d) $50^1_0 52^1_0$, and (e) $50^1_0 51^1_0$. Transitions which serve as false origins are marked with a red (0^0_0).

is shown in Fig. 10c and d, respectively. The presence of Fermi resonant mixing between the pair of excited state levels is manifested by the $\Delta\nu = 0$ emission to both the $50_1 51_1$ and 34_1 ground state levels appearing in both DFL spectra. Oddly enough, the $50^1_1 51^1_1$ transition is the only observed case in which a fully $\Delta\nu = 0$ transition is even observed in the DFL spectra of these out-of-plane combination levels. Nonetheless, the presence of this $\Delta\nu = 0$ transition has enabled a quantitative analysis of the Fermi resonance mixing coefficients, α and β with $\alpha = 0.802$ and $\beta = 0.597$. Using these expansion coefficients, the calculated Franck–Condon integrals reproduce, with high fidelity, the relative peak intensities observed in the DFL spectra. See Section S8 (ESI†) for details.

B. Methyl anthranilate–water complex

1. Computational predictions. Complexation of a single water molecule to MA (MA–H_2O) can occur at several binding sites, supporting numerous conformers. At the DFT B3LYP-D3BJ/def2TZVP level of theory we have calculated seven minima lying within 10 kJ mol^{-1} of the global energy minimum (see Fig. S13 and Table S1, ESI†). In each of these structures, the monomer portion adopts the same rotamer form that we have just assigned, *i.e.*, with the amine group hydrogen bonded with the carbonyl group. None of the conformers have symmetry in their calculated S_0 or S_1 states. This is not due, as was the case in the MA S_0 geometry, to a symmetric double well potential along the NH_2 inversion coordinate, but rather the H_2O molecule asymmetrically binding to the MA monomer unit with an out-of-plane position for its center-of-mass. The calculated equilibrium structure of the assigned MA–H_2O complex in its S_0 and S_1 geometry is shown in Fig. 11. This conformer was calculated to be the zero-point corrected energy minimum both with and without basis set superposition error (BSSE) correction (see Fig. S13 and Table S1, ESI†).

The loss of symmetry upon water complexation means that the in-plane/out-of-plane selection rules present in MA monomer are no longer present in the complex. As we shall see, however, the relative intensities of certain bands in the excitation spectrum suggest a weakening of these selection rules rather than a binary switch between on and off. The 63 normal modes of vibration of the complex are designated with the Mulliken scheme, from high to low frequency. Nevertheless, many of the MA vibrations retain much of their character upon water complexation, and we refer to this connection in what follows. Formally speaking, six new intermolecular vibrations are associated with hindered translation (3) and rotation (3) of the H_2O molecule relative to MA.

Vertical TD-DFT B3LYP-D3BJ/def2TZVP calculations predict that the S_1 electronic state of MA–H_2O is very similar to its character in MA monomer, with a nearly-identical form for the molecular orbitals and their coefficients in the S_0–S_1 transition. The S_2 and S_3 states are now nearly isoenergetic with one another at the ground state geometry, lying 1.31 eV and 1.34 eV above S_1. Interestingly, the S_0–S_2 and S_0–S_3 electronic transitions now involve both $n\pi^*$ and $\pi\pi^*$ single electron transitions. The MOs associated with these transitions are shown in ESI† (Section S10). Despite these differences, the large energy separation of S_1 from S_2/S_3 and smaller oscillator strength makes it unlikely that vibronic coupling will be manifested in the S_0–S_1 vibronic spectrum of the complex.

2. UV excitation spectroscopy. The labelled IR-UV HB spectrum of MA–H_2O is shown in Fig. 12. The spectrum spans from 28 500–30 000 cm^{-1}, with the S_0–S_1 electronic origin transition appearing at 28 574 cm^{-1}, shifted 278 cm^{-1} to the red of the MA monomer origin due to the relative water binding energies in the S_0 and S_1 states. The lifetime of the S_1 state is measured to be 23 ns, very close to that of the monomer (see Fig. S8b for the fluorescence decay trace, ESI†). The MA–H_2O assignments included in Fig. 12 were reached based on corroborating evidence from S_0 and S_1 vibrational frequency calculations, zero-point energy calculations, excitation and DFL spectra (discussed below). Progressions in modes ν_{56} (187 cm^{-1}) and ν_{49} (427 cm^{-1}) are displayed *via* dotted tie-lines, while combination bands built off of 49^1_0 are shown with solid tie-lines. All other assigned peaks are labelled with tags.

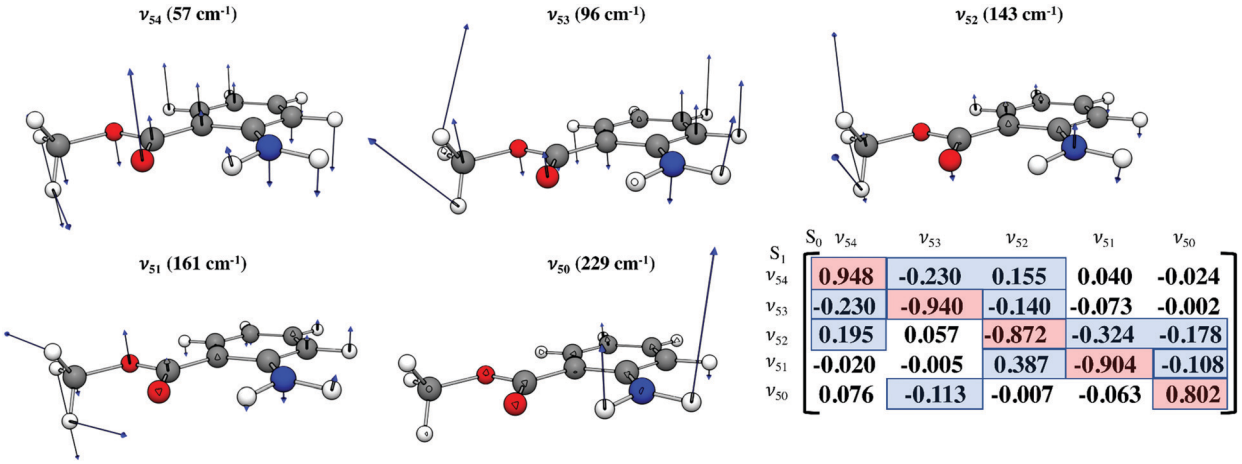

S_1 \ S_0	ν_{54}	ν_{53}	ν_{52}	ν_{51}	ν_{50}
ν_{54}	0.948	-0.230	0.155	0.040	-0.024
ν_{53}	-0.230	-0.940	-0.140	-0.073	-0.002
ν_{52}	0.195	0.057	-0.872	-0.324	-0.178
ν_{51}	-0.020	-0.005	0.387	-0.904	-0.108
ν_{50}	0.076	-0.113	-0.007	-0.063	0.802

Fig. 9 Ground state out-of-plane normal modes ν_{54}–ν_{50} of MA, along with the reduced Duschinsky matrix of these modes. The matrix row elements give the expansion coefficients of the indicated S_1 normal coordinate in terms of the S_0 coordinates. The normal modes and Duschinsky matrix were calculated at the DFT B3LYP-D3BJ/def2TZVP level of theory.

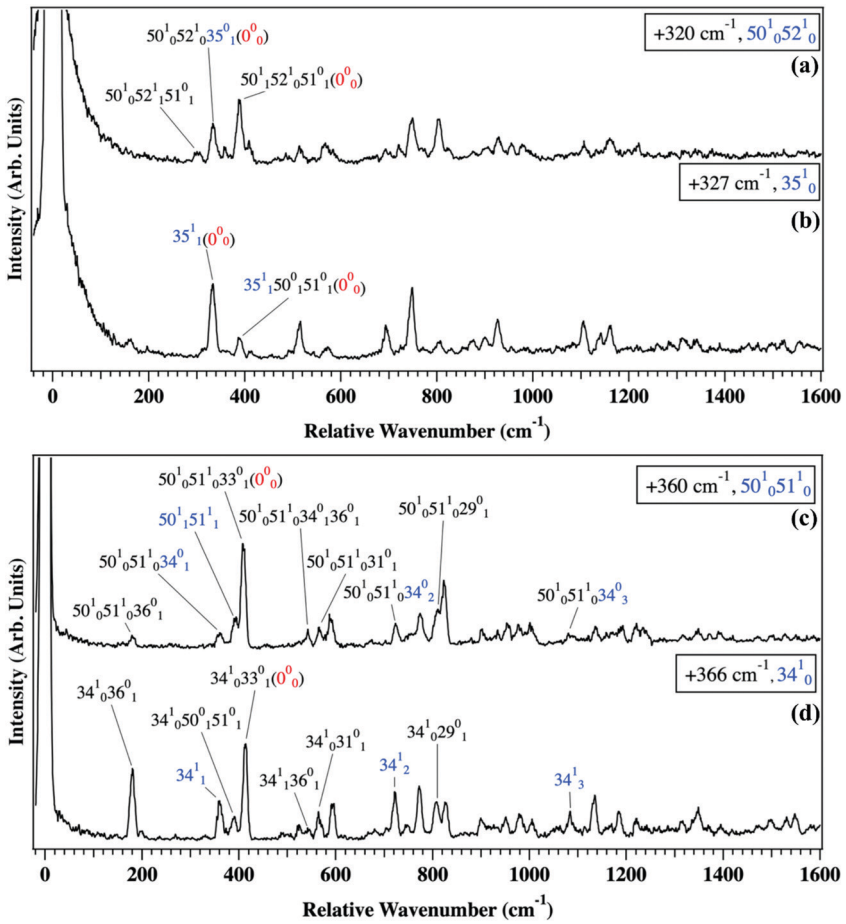

Fig. 10 DFL of Fermi resonance modes (a) $50^1_0 52^1_0$ and (b) 35^1_0, and (c) $50^1_0 51^1_0$ and (d) 34^1_0 of MA. Ground state transitions to Fermi-mixed components are labelled in blue text, and transitions which serve as false origins are marked with a red (0^0_0).

The Franck–Condon activity present in Fig. 12 bears some resemblance to that in MA monomer, most notably in the progressions of ν_{56} and ν_{49}, which have their corresponding modes at similar frequencies in MA monomer (ν_{36}, 179 cm^{-1} and ν_{33}, 421 cm^{-1}, respectively). Table 2 lists the experimental and calculated MA–H_2O S_0 and S_1 vibrational frequencies, along with their corresponding MA values. We note the presence of several analogous MA Franck-Condon active modes

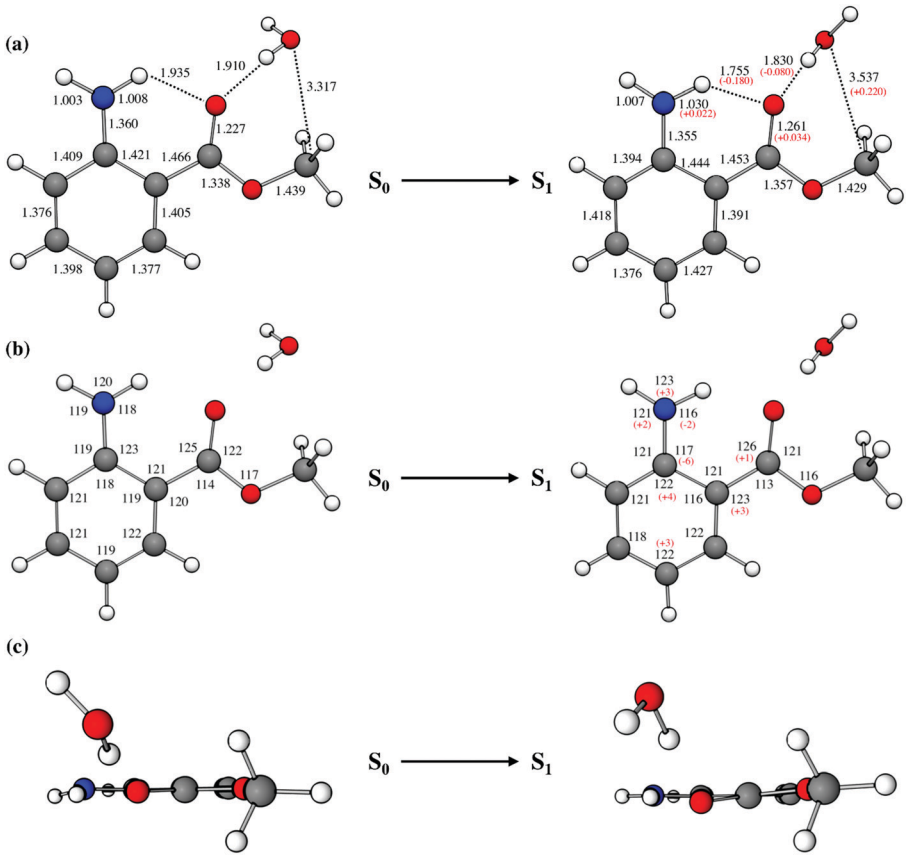

Fig. 11 Optimized ground and S_1 excited state geometries of MA–H_2O with (a) bond distances and (b) bond angles labelled, and (c) a side view showing the change in water position upon electronic excitation. Bond lengths are in angstroms (Å) and angles are in degrees. The difference between select ground and excited state parameters are shown in red parentheses. Values were calculated at the DFT B3LYP-D3BJ/def2TZVP level of theory.

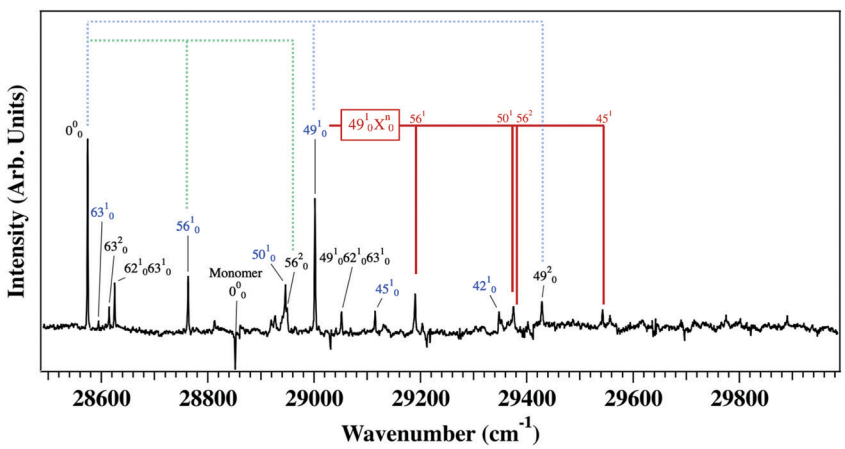

Fig. 12 Assigned S_0–S_1 LIF excitation spectrum of MA–H_2O. Progressions in the in-plane modes ν_{56} (189 cm^{-1}), and ν_{49} (427 cm^{-1}) are displayed *via* green and blue dotted tie-lines, respectively, while in-plane combination bands built off 49^1_0 are shown with solid tie lines. The identity of mode X is listed above each respective tie line.

in the vibronic spectra of MA–H_2O. In many cases the frequencies increase in the presence of H_2O, indicating some stiffening of these in-plane vibrations (shown in Fig. S18, ESI†) when H_2O is present.

The triad of peaks immediately after the origin transition show an interesting intensity pattern, with each member of the triad more intense as frequency increases. If in both electronic states the geometry of MA–H_2O is non-planar, then one might expect to see large Franck–Condon activity in modes with mostly out-of-plane character. Instead, what we observe is the overtone of ν_{63} (63^2_0) being three times as intense as its fundamental transition (63^1_0), and the $62^1_0 63^1_0$ combination band twice again as

Table 2 Experimental and calculated S_0 and S_1 frequencies of MA–H_2O[a]

S_0			S_1	
Mode	Exp. freq. (cm^{-1})	Calc. freq.[b] (cm^{-1})	Exp. freq. (cm^{-1})	Calc. freq.[b] (cm^{-1})
63	9	10	20	22
62	49	50	31	33
56 (36)	187 (179)	185	189 (179)	189
50 (34)	345 (361)	360	372 (366)	362
49 (33)	418 (412)	428	427 (421)	426
45 (31)	568 (567)	573	541 (540)	560
42 (30)	667 (672)	684	773 (610)	789
38 (29)	817 (808)	821	— (773)	789
23 (18)	1363 (1355)	1355	—	1382

[a] Values in parentheses are analogous values of MA. [b] Frequencies calculated at the DFT B3LYP-D3BJ/def2TZVP level of theory.

intense as the 63_0^2 overtone. Both mode 62 and 63 are primarily intermolecular vibrations of the H_2O molecule, with ν_{63} mostly an out-of-plane motion (see Fig. S18, ESI†). These relative intensities suggest that the MA–H_2O complex retains a weakened form of its C_s selection rules in the complex; not surprisingly so, given that the electronic transition is localized on the planar MA monomer. As a result, the even overtone and 1 + 1 combination band are favored over the 63_0^1 out-of-plane intermolecular fundamental.

3. Origin DFL spectrum. The assigned DFL spectrum of the 0_0^0 transition of MA–H_2O is shown in Fig. 13. As with MA, this spectrum generally mirrors that of the MA–H_2O excitation spectrum, reflecting that Franck–Condon factors between the S_0 and S_1 electronic states of MA largely dictate the vibronic structure in both excitation and emission. The same two modes that were Franck–Condon active in the excitation spectrum, ν_{56} and ν_{49}, also appear as progressions in the DFL spectrum. Mode 49 is also an active member in combination band transitions.

The low frequency $62_1^0 63_1^0$ combination band at 58 cm^{-1} in the 0^0 DFL spectrum is the analogous combination band transition that we observed in the excitation spectrum ($62_0^1 63_0^1$). Due to the presence of intense laser scatter, we are not able to see whether this DFL spectrum contains the analogous 63_1^0 and 63_2^0 transitions that appeared in the excitation spectrum. It is worth noting that the ground state modes 62 and 63 are substantially mixed with one another in S_1, as revealed by large off-diagonal components in the Duschinsky matrix (see Fig. S18, ESI†). Several of the modes present in the excitation spectrum appears in the DFL spectrum with analogous $\Delta\nu = 1$ transitions. Similarly, one higher frequency band is present in the DFL spectrum, ν_{23}, appearing at 1363 cm^{-1}. This mode is analogous to ν_{18} in MA (see Table 2).

IV. Discussion

A. Structural changes associated with hydrogen atom dislocation

The Franck–Condon activity in several in-plane modes in the excitation and DFL spectra of MA indicate that the molecular geometries in the S_0 and S_1 states differ substantially from one another along these coordinates. We have carried out a near-complete assignment of the vibrationally-resolved LIF excitation scan and an array of DFL spectra out of single vibronic levels in the excited state. In all cases, the unscaled harmonic vibrational frequencies predicted by the DFT and TDDFT calculations at the B3LYP-D3BJ/def2TZVP level of theory closely reproduce the experimental values, with an average error of ±10.5 cm^{-1}. Furthermore, the rotational constants and transition dipole

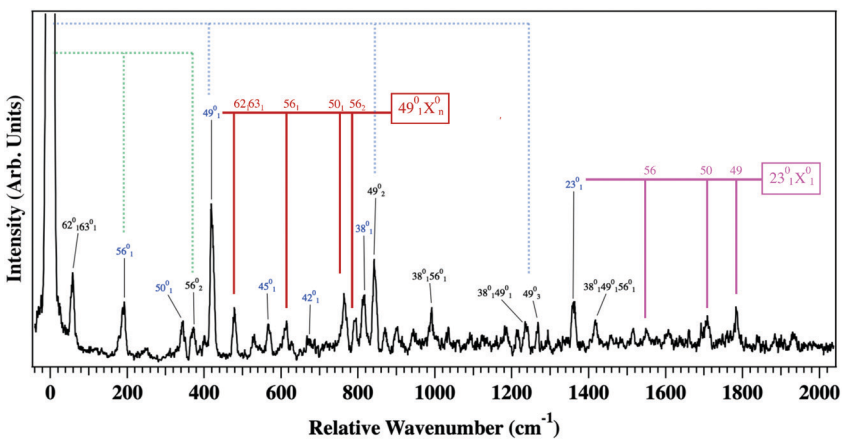

Fig. 13 Dispersed fluorescence spectrum of the S_0–S_1 origin transition of MA–H_2O. Progressions in the in-plane modes ν_{56} (187 cm^{-1}) and ν_{49} (418 cm^{-1}) are displayed *via* green and blue dotted tie-lines, respectively, while in-plane combination bands built off 49_1^0 and 23_1^0 are shown with solid tie lines. The identity of mode X is listed above each respective tie line.

moment direction from calculation faithfully reproduce the rotational band contour of the electronic origin without adjustment. This leads to the conclusion that the calculations faithfully reproduce the ground state and excited state potential energy surfaces around the S_0 and S_1 minima, and therefore are anticipated to be trustworthy in the more detailed structural changes accompanying electronic excitation.

From an experimental viewpoint, while all the low-frequency in-plane vibrations have some Franck–Condon activity, longer progressions extending to $\nu' = 3$ in modes 36 and 33, and $\nu' = 2$ in mode 34 are evident in the 0^0 DFL spectrum (Fig. 5), reflecting largest geometry changes along these vibrational coordinates. Indeed, the majority of the vibronic structure in the excitation and DFL spectra can be accounted for as progressions and combination bands involving these three modes. These three modes all involve substantial in-plane motion of the NH_2 and CO_2Me groups relative to one another. These heavy atom motions modulate the average distance between the H-bonded NH donor and the carbonyl oxygen acceptor groups along what might be termed the 'reaction coordinate' for a hydrogen atom transfer or dislocation. In a separate paper, we will view these effects on the interactions between the NH and C═O groups more directly by presenting infrared spectra of MA and MA–H_2O in the NH stretch, NH bend, and C═O stretch regions in both S_0 and S_1 states.[33]

The low-frequency Franck–Condon activity that is the subject of the present work gives insight principally on the heavy atom motions that accompany electronic excitation. MA affords the opportunity to view this structural change by projecting a range of excited state vibrational levels back onto the ground state *via* their dispersed emission. As a result, armed with a comprehensive assignment of the electronic spectra, we now turn to a more detailed discussion of the structural change associated with the $\pi\pi^*$ electronic excitation, based on the optimized geometries shown in Fig. 2.

In MA, the optimized ground state geometry has as its most characteristic feature the intramolecular H-bond between the NH_2 and C═O groups, with a H-bond distance of 1.926 Å associated with a short, but bent H-bond. This places the NH_2 group in an unusual situation in that amines are known most for their role as good H-bond acceptors due to the lone pair on the N atom, not as H-bond donors. Nevertheless, in the ground state, the structural effects of the NH···O═C H-bond are modest, with neither the NH nor C═O bond lengths being changed significantly from their ground state bond values in the singly-substituted analogs aniline (NH_2 only, $\Delta R = +0.001$ Å) or methyl benzoate (methyl ester only, $\Delta R = +0.012$ Å), both of which lack the intramolecular H-bond. Sections S12 and S13 (ESI†) show calculated S_0 and S_1 structures of aniline and methyl benzoate.

The structural changes associated with electronic excitation are more dramatic. The primary changes involve structural distortions and positional changes in the NH_2 group relative to the methyl ester. First, the N–H_{donor} and O═C bonds each increase in length by ~0.03 Å, characteristic changes associated with strengthening a H-bond between them. Second, the NH bond rotates towards the carbonyl oxygen, closing the CNH bond angle by 2°. Third, the CCN bond angle decreases from 122° to 116°. Taken together, these structural changes tilt and stretch the NH_2 group toward the methyl ester, contracting the 6-membered (C6) ring that is closed by the NH···O═C hydrogen bond. This results in a substantial decrease of the H···O hydrogen bonding distance by 0.203 Å, taking what is already a short H-bond ($R_{H\cdots O}$ = 1.926 Å) and making it extraordinarily short ($R_{H\cdots O}$ = 1.723 Å). Nearly identical structural changes occur in MA–H_2O upon electronic excitation. One interesting difference, however, is that the H···O distance decreases by 0.02 Å less in MA–H_2O than in MA. This is likely a result of the electronegative C═O oxygen acting as H-bond acceptor to both the NH and water OH, thereby decreasing its affinity for the dislocated NH. Table 3 lists the S_0, S_1, and difference in structural parameters for MA and MA–H_2O.

In previous work on anthranilic acid, the excited state structural change was labeled as a 'hydrogen-atom dislocation' to indicate its partial nature, as distinct from 'hydrogen-atom transfer', in which a hydrogen atom is completely transferred from one nucleus to another.[15] For further comparison of the anthranilates upon electron excitation, see Section S14 (ESI†). As we will discuss in more detail in the following section, in salicylic acid and similar molecules, the transfer involves O–H bond lengthening, with relaxation along several heavy-atoms on the S_1 potential energy surface and subsequent red-shifted emission and/or non-radiative decay *via* an S_1/S_0 conical intersection (CI).[2–4,12] In MA, we have investigated the S_0–S_1 Franck–Condon active region, and see no evidence of hydrogen atom transfer near the S_1 origin. This is demonstrated by the absence of non-radiative processes in the UV-D spectrum, and the lack of strongly red-shifted emission in the DFL spectra.

What the present study has achieved is a deeper understanding of what 'hydrogen atom dislocation' means in methyl anthranilate. As just summarized, the optimized excited state structure has an H···O distance 0.203 Å shorter than in the ground state, with $R_{H\cdots O}$ = 1.723 Å. If full transfer were to shorten this distance to 1.0 Å, then the dislocation in MA is about 25% of full transfer. However, only 0.03 Å of this dislocation involves

Table 3 Structural parameters of MA and MA–H_2O[a]

	Methyl anthranilate			Methyl anthranilate:H_2O		
	S_0	S_1	Δ	S_0	S_1	Δ
R_{C-N}[b]	1.359	1.356	−0.003	1.360	1.355	−0.005
$R_{N-H_{donor}}$	1.008	1.035	0.027	1.008	1.030	0.022
$R_{N-H_{free}}$	1.003	1.007	0.004	1.003	1.007	0.004
θ_{H-N-H}[c]	120°	124°	4°	120°	123°	3°
D_{CNHH}	0°	0°	0°	11°	3°	−8°
$R_{C=O}$	1.220	1.252	0.032	1.227	1.261	0.034
R_{C-O}	1.349	1.364	0.015	1.338	1.357	0.019
$\theta_{O=C-O}$	121	121°	0°	122°	121°	−1°
$R_{H\cdots O}$	1.926	1.723	−0.203	1.935	1.755	−0.180
$\theta_{N-H_{donor}-O}$	130°	141°	11°	129°	139°	10°
R_{OH-O}	—	—	—	1.910	1.830	−0.080
R_{HO-C}	—	—	—	3.317	3.537	0.220
$\theta_{O-H\cdots O}$	—	—	—	171°	178°	7°

[a] Structures calculated at the DFT B3LYP-D3BJ/def2TZVP level of theory. [b] Distances in Å. [c] Angles in degrees.

lengthening the NH bond, while the remaining 0.173 Å is due to the heavy atom motion just described that reorients the entire NH_2 group relative to the C═O acceptor. Further details of the Franck–Condon analysis involving vibrational motions of the NH_2 and COOMe is included in ESI† (Section S15).

B. Photophysical properties of MA and implications as a sunscreen precursor

MA is the precursor to menthyl anthranilate (MenA), an FDA approved sunscreen agent. Rodrigues *et al.* have recently shown, in both condensed- and gas-phase, that MA and MenA exhibit nearly identical photochemical/photophysical properties.[13] In order to put the absorption and photophysical properties of MA in proper context, we compare MA first to its simpler analogs, aniline (NH_2 substitution only) and methyl benzoate (CO_2Me substitution only).

Aniline is a prototypical aromatic amine that has been studied extensively. Its S_0–S_1 origin appears at 34 025 cm^{-1}, and is readily detected by both fluorescence and R2PI schemes.[34–38] Using the same level of theory as in MA, we calculated S_0 and S_1 state optimized geometries for aniline (shown in Fig. S19, ESI†). The S_0–S_1 transition of aniline is a prototypical ππ* transition for a phenyl derivative, leading to expansion in the size of the aromatic ring, modest shortening of the CN bond (ΔR_{CN} = −0.026 Å), and planarization of the NH_2 group in the S_1 state.

Methyl benzoate (MB), by contrast, has its S_0–S_2 transition (the first optically accessible singlet ππ* state, see Section S13, ESI†) at 36 105 cm^{-1}, but cannot be detected either in LIF or R2PI due to fast intersystem crossing (ISC) to the nπ* triplet state that shortens the excited state lifetime and reduces the fluorescence quantum yield. Its spectroscopy has been studied using sensitized phosphorescence detection.[39] Table 4 shows the energetic ordering of electronic states of aniline, MB, MA, and MA–H_2O. The calculated structural changes associated with electronic excitation (shown in Fig. S20, ESI†) include expansion in the size of the aromatic ring, substantial lengthening of the C═O bond ($\Delta R_{C=O}$ = +0.110 Å) and a closing of the O═C–O angle ($\Delta\theta_{O=C-O} = -10^{\circ}$).

Inclusion of both methoxycarbonyl and amine groups as *ortho*-ring substituents in MA modifies the properties of the singly-substituted molecules in several ways. The absorbing states are redshifted from the UV-B (280–315 nm) region (276.9 nm in MB and 293.9 nm in aniline) into the UV-A region (315–400 nm), with S_0–S_1 origin at 346.9 nm and low-frequency Franck–Condon activity stretching to 333.3 nm in the gas phase (see Fig. 14 for the molecular orbitals involved in the S_0–S_1 transitions in MA). The TDM vectors of the bright transitions of MB and Aniline essentially add to form the TDM vector in MA, with the oscillator strength of the MA nearly tripling that of aniline and increasing by nearly an order of magnitude in MB, respectively (see Fig. S25, ESI†).

Relative to MB, MA's inclusion of the amine group reorders the electronic states substantially. In MB, the ester C═O group gives rise to a triplet nπ* state that, according to calculations, lies 4033 cm^{-1} (0.5 eV) below the absorbing singlet ππ* state (see Table 4). In accordance with El-Sayed's rule, ^{1}ππ* ↔ ^{3}nπ* ISC is efficient when energetically allowed, producing an experimentally observed long-lived non-fluorescent state.[39] The strong intramolecular hydrogen bond in MA, which includes bonding of the C═O lone electron pair, results in an increase in energy of the nπ* state relative to the ππ* state. According to calculations, this raises the energy of the triplet nπ* state to 6210 cm^{-1} (0.77 eV) above that of the absorbing singlet ππ* state. The destabilization of the triplet nπ* state in MA removes the possibility of ISC involving that state.

The lack of formation of long-lived, reactive, triplet state species upon photoexcitation of MA is in accordance with its having the same electronic chromophore as active sunscreen agents. On the other hand, effective sunscreens typically undergo efficient non-radiative decay from the excited state back to the ground state, thereby recycling their UV-absorption capacity. In several of these molecules, excited-state deactivation is thought to be facilitated by H-atom transfer on the S_1 surface,[3,4,40] in some cases followed by transient C═C bond rotation, at which geometries the S_1 and S_0 surfaces meet at a conical intersection.[5–7,40–42] Internal conversion, accompanied by hydrogen atom back-transfer, restores the molecule to the ground electronic state configuration. Alternatively, as is thought to be the case with salicylic acid and methyl salicylate, the H-atom transferred excited state may become trapped in a local minimum on the S_1 surface, resulting in Stokes-shifted emission.[3,4,9,10]

Our characterization of the excited state of MA agrees with results from a recent time-domain study of MA by Rodriguez *et al.* where they presented experimental and computational evidence indicating that a complete hydrogen atom transfer from a region near the S_1 origin is endothermic.[13] These authors computed a two-step, endothermic (no bound intermediates) pathway toward a conical intersection, involving motion along a

Table 4 Electronic states in aniline, methyl benzoate, methyl anthranilate, and methyl anthranilate–H_2O[a]

Aniline			Methyl benzoate			Methyl anthranilate			Methyl anthranilate–H_2O		
State	Energy (eV)	f_{0n}	State	Energy (eV)	f_{0n}	State	Energy (eV)	f_{0n}	State	Energy (eV)	f_{0n}
^{3}ππ*	3.65	0.0000	^{3}ππ*	3.57	0.0000	^{3}ππ*	3.03	0.0000	^{3}ππ*	2.95	0.0000
^{3}ππ*	3.86	0.0000	^{3}ππ*	4.18	0.0000	^{3}ππ*	3.56	0.0000	^{3}ππ*	3.50	0.0000
^{3}ππ*	4.49	0.0000	^{3}nπ*	4.47	0.0000	^{1}ππ*	3.92	0.1036	^{1}ππ*	3.84	0.1077
^{1}ππ*	4.75	0.0359	^{3}ππ*	4.53	0.0000	^{3}ππ*	4.17	0.0000	^{3}ππ*	4.12	0.0000
^{3}ππ*	5.32	0.0000	^{1}nπ*	4.88	0.0001	^{3}nπ*	4.69	0.0000	^{3}nπ*	4.81	0.0000
^{3}ππ*	5.40	0.0000	^{1}ππ*	4.97	0.0153	^{1}nπ*	5.08	0.0002	^{1}nπ*/ππ*	5.15	0.0530
^{1}ππ*	5.42	0.0644	^{3}ππ*	5.07	0.0000	^{1}ππ*	5.23	0.0481	^{1}nπ*/ππ*	5.18	0.0117

[a] Values calculated at the DFT B3LYP-D3BJ/def2TZVP level of theory.

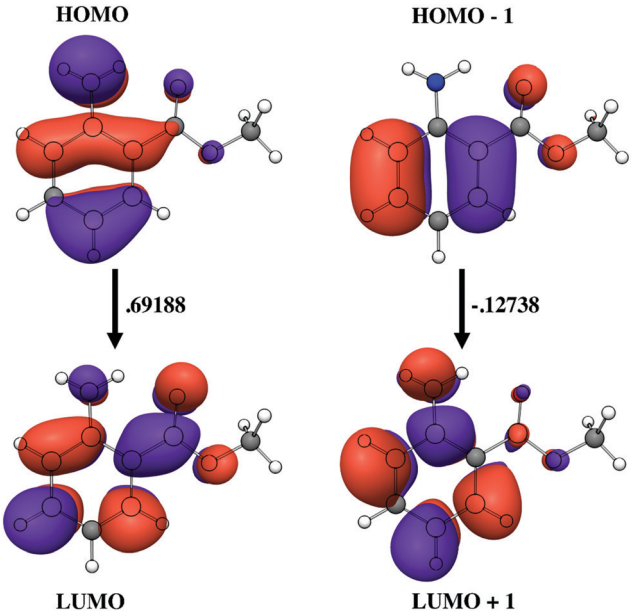

Fig. 14 Molecular orbitals (MO) transitions comprising the S_0–S_1 transition of MA, along with their coefficients. Additional MOs of molecules discussed herein are presented in the supporting information. Calculations were carried out at the DFT B3LYP-D3BJ/def2TZVP level of theory.

1700 cm^{-1} barrier to an unbound hydrogen atom transfer geometry followed by a 3200 cm^{-1} barrier to ester group (C═C) rotation, at which geometry S_1 and S_0 curves meet at a CI. In a follow up study, they observed damping of time-dependent quantum beat signals upon irradiation centered at 315 nm, at photoexcitation energies ~1200 cm^{-1} above the H-atom transfer barrier (2000 cm^{-1} below the CI barrier), which they attributed to the rapid redistribution of energy *via* IVR.[43] This is in good agreement with our observation of broadened DFL scans occurring in the excited state of MA with only ~800 cm^{-1} excess energy, at which the density of S_1 vibrational states is calculated to be 14 states/cm^{-1}.[43] Their time- and our frequency-resolved data indicate that, in the S_0–S_1 Franck–Condon active region, while the structural changes associated with electronic excitation would seem to facilitate H-atom transfer, there exists no bound intermediate on the excited state surface on which the tautomer product can exist. Taken as a whole, the excited state properties of methyl anthranilate near the S_0–S_1 origin show no fast non-radiative pathways that one typically associates with efficient sunscreens. The same is likely true of menthyl anthranilate, bolstering the case for rational sunscreen design.

V. Conclusion

We have presented the LIF excitation and dispersed fluorescence spectra of methyl anthranilate, leading to assignment of nearly every vibronic transition in the first ~1000 cm^{-1} of the excitation and DFL spectra. The observed transitions prove that MA retains C_s symmetry in both its S_0 and S_1 states. The presence of cross-sequence bands in the DFL spectra of MA indicate a high degree of Duschinsky mixing between S_0 and S_1 states involving both out-of-plane and in-plane normal modes. The presence of so many in-plane normal modes in the vibronic spectra indicate a displacement of their respective normal mode coordinates upon electronic excitation, and reflect a significant change in geometry upon electronic excitation. More importantly, the spectrum is dominated by Franck–Condon progressions involving three low-frequency in-plane modes (ν_{33}, ν_{34}, and ν_{36}) that modulate the distance between the NH_2 and CO_2Me groups during their vibrational motion.

A combination of experimental and corroborating computational evidence provides a more detailed picture of this structural change, identifying it as a rocking and re-orientation of the NH_2 and CO_2Me groups that brings them closer to one another, thereby strengthening the six-membered hydrogen bonded ring between the two groups. In particular, upon electronic excitation, the H···O hydrogen bonding distance decreases by 0.203 Å to a value of just 1.723 Å. Since a full H-atom transfer would result in an O–H bond of about 1.0 Å, the 0.20 Å shortening is aptly labeled as a hydrogen-atom dislocation, although it is largely the heavy atoms that rearrange to close the transfer distance, since the N–H_{donor} bond distance increases by only 0.027 Å. At the same time, the process is far short of a complete hydrogen atom transfer. Indeed, as the UV-D and DFL spectra indicate, in the Franck–Condon active region, the changes in MA associated with electronic excitation are primarily structural and not non-radiative.

We have also presented LIF excitation and 0_0^0 DFL spectra for the MA–H_2O complex. In the assigned structure, the water molecule hydrogen bonds to the 'back side' of the C═O group weakening but not disrupting the intramolecular NH···O═C H-bond. As a result, much of the Franck–Condon activity associated with the electronic transition is retained in the complex.

While this paper has focused attention on the electronic spectroscopy of MA and MA–H_2O, infrared spectroscopy can provide a complementary probe of the pre-reactive structural changes. In fact, the NH, OH, and C═O oscillators serve as sensitive reporters of their local environments. In an upcoming paper, we build upon our results here by reporting on the hydride stretch and mid-infrared spectra of MA and MA–H_2O in both ground and excited states.

Conflicts of interest

There are no conflicts to declare.

Acknowledgements

KNB, DS, JLF, and TSZ gratefully acknowledge support for this work from the National Science Foundation under grant NSF-CHE1764148. ELS acknowledge support from the National Science Foundation under grant NSF-CHE-1566108.

References

1 A. Beeby and A. E. Jones, *Photochem. Photobiol.*, 2000, **72**, 10–15.
2 T. N. V. Karsili, B. Marchetti, M. N. R. Ashfold and W. Domcke, *J. Phys. Chem. A*, 2014, **118**, 11999–12010.

3 A. L. Sobolewski and W. Domcke, *Phys. Chem. Chem. Phys.*, 2006, **8**, 3410–3417.
4 P. B. Bisht, H. Petek, K. Yoshihara and U. Nagashima, *J. Chem. Phys.*, 1995, **103**, 5290–5307.
5 Y. Peperstraete, M. Staniforth, L. A. Baker, N. D. N. Rodrigues, N. C. Cole-Filipiak, W.-D. Quan and V. G. Stavros, *Phys. Chem. Chem. Phys.*, 2016, **18**, 28140–28149.
6 L. A. Baker, M. D. Horbury, S. E. Greenough, P. M. Coulter, T. N. Karsili, G. M. Roberts, A. J. Orr-Ewing, M. N. Ashfold and V. G. Stavros, *J. Phys. Chem. Lett.*, 2015, **6**, 1363–1368.
7 N. D. Rodrigues, M. Staniforth and V. G. Stavros, *Proc. R. Soc. A*, 2016, **472**, 20160677.
8 L. A. Baker, B. Marchetti, T. N. Karsili, V. G. Stavros and M. N. Ashfold, *Chem. Soc. Rev.*, 2017, **46**, 3770–3791.
9 L. Heimbrook, J. E. Kenny, B. E. Kohler and G. W. Scott, *J. Phys. Chem.*, 1983, **87**, 280–289.
10 L. A. Heimbrook, J. E. Kenny, B. E. Kohler and G. W. Scott, *J. Chem. Phys.*, 1981, **75**, 5201–5203.
11 J. Zhao, S. Ji, Y. Chen, H. Guo and P. Yang, *Phys. Chem. Chem. Phys.*, 2012, **14**, 8803–8817.
12 T. Raeker and B. Hartke, *J. Phys. Chem. A*, 2017, **121**, 5967–5977.
13 N. D. N. Rodrigues, N. C. Cole-Filipiak, M. D. Horbury, M. Staniforth, T. N. V. Karsili, Y. Peperstraete and V. G. Stavros, *J. Photochem. Photobiol., A*, 2018, **353**, 376–384.
14 J. A. Stearns, A. Das and T. S. Zwier, *Phys. Chem. Chem. Phys.*, 2004, **6**, 2605–2610.
15 C. A. Southern, D. H. Levy, G. M. Florio, A. Longarte and T. S. Zwier, *J. Phys. Chem. A*, 2003, **107**, 4032–4040.
16 A. L. Sobolewski and W. Domcke, *J. Phys. Chem. A*, 2004, **108**, 10917–10922.
17 E. A. E.-H. Abou El-Nasr, A. Fujii, T. Yahagi, T. Ebata and N. Mikami, *J. Phys. Chem. A*, 2005, **109**, 2498–2504.
18 S. Leśniewski, P. Kolek, K. Pirowska, A. L. Sobolewski and J. Najbar, *J. Chem. Phys.*, 2009, **130**, 054307.
19 P. Kolek, M. Andrzejak, R. Hakalla and W. Szajna, *J. Phys. Chem. A*, 2018, **122**, 6243–6255.
20 N. R. Pillsbury, C. W. Muller, W. L. Meerts, D. F. Plusquellic and T. S. Zwier, *J. Phys. Chem. A*, 2009, **113**, 5000–5012.
21 S. Grimme, *J. Comput. Chem.*, 2004, **25**, 1463–1473.
22 S. Grimme, *J. Chem. Phys.*, 2006, **124**, 034108.
23 M. Frisch, G. Trucks, H. Schlegel, G. Scuseria, M. Robb, J. Cheeseman, G. Scalmani, V. Barone, G. Petersson and H. Nakatsuji, *Revision A*, 2016, vol. 3.
24 G. Zhurko and D. Zhurko, 2009, URL: http://www.chemcraftprog.com.
25 P. Butler, D. B. Moss, H. Yin, T. W. Schmidt and S. H. Kable, *J. Chem. Phys.*, 2007, **127**, 094303.
26 R. S. Mulliken, *J. Chem. Phys.*, 1955, **23**, 1997–2011.
27 D. F. Plusquellic, R. Suenram, B. Mate, J. Jensen and A. Samuels, *J. Chem. Phys.*, 2001, **115**, 3057–3067.
28 F. Duschinsky, *Acta Physicochim. URSS*, 1937, **7**, 551–566.
29 C. W. Muller, J. J. Newby, C.-P. Liu, C. P. Rodrigo and T. S. Zwier, *Phys. Chem. Chem. Phys.*, 2010, **12**, 2331–2343.
30 J. B. Hopkins, D. E. Powers and R. E. Smalley, *J. Chem. Phys.*, 1980, **72**, 5039–5048.
31 J. B. Hopkins, D. E. Powers, S. Mukamel and R. E. Smalley, *J. Chem. Phys.*, 1980, **72**, 5049–5061.
32 C.-P. Liu, J. J. Newby, C. W. Müller, H. D. Lee and T. S. Zwier, *J. Phys. Chem. A*, 2008, **112**, 9454–9466.
33 K. N. Blodgett, J. L. Fischer, D. Sun, E. L. Sibert III and T. S. Zwier, 2019, manuscript in preparation.
34 N. Mikami, A. Hiraya, I. Fujiwara and M. Ito, *Chem. Phys. Lett.*, 1980, **74**, 531–535.
35 M. Quack and M. Stockburger, *J. Mol. Spectrosc.*, 1972, **43**, 87–116.
36 E. R. T. Kerstel, M. Becucci, G. Pietraperzia, D. Consalvo and E. Castellucci, *J. Mol. Spectrosc.*, 1996, **177**, 74–78.
37 J. H. Brophy and C. T. Rettner, *Chem. Phys. Lett.*, 1979, **67**, 351–355.
38 J. T. Meek, E. Sekreta, W. Wilson, K. Viswanathan and J. P. Reilly, *J. Chem. Phys.*, 1985, **82**, 1741–1749.
39 S. Kamei, H. Abe, N. Mikami and M. Ito, *J. Phys. Chem.*, 1985, **89**, 3636–3641.
40 T. N. Karsili, B. Marchetti, M. N. Ashfold and W. Domcke, *J. Phys. Chem. A*, 2014, **118**, 11999–12010.
41 K. Yamazaki, Y. Miyazaki, Y. Harabuchi, T. Taketsugu, S. Maeda, Y. Inokuchi, S.-N. Kinoshita, M. Sumida, Y. Onitsuka and H. Kohguchi, *J. Phys. Chem. Lett.*, 2016, **7**, 4001–4007.
42 S.-N. Kinoshita, Y. Miyazaki, M. Sumida, Y. Onitsuka, H. Kohguchi, Y. Inokuchi, N. Akai, T. Shiraogawa, M. Ehara and K. Yamazaki, *Phys. Chem. Chem. Phys.*, 2018, **20**, 17583–17598.
43 N. D. N. Rodrigues, N. C. Cole-Filipiak, K. N. Blodgett, C. Abeysekera, T. S. Zwier and V. G. Stavros, *Nat. Commun.*, 2018, **9**, 5188.